Nuclear Instruments and Methods in Physics Research A 1068 (2024) 169707

Contents lists available at ScienceDirect

Nuclear Inst. and Methods in Physics Research, A

journal homepage: www.elsevier.com/locate/nima

Full Length Article

Amorphous carbon-coated storage cell tests for the polarized gas target at LHCb

T. El-Kordy [a,b,c,*], P. Costa Pinto [d], P. Di Nezza [e], R. Engels [a,b], M. Ferro-Luzzi [d], N. Faatz [a,b,f], K. Grigoryev [b], C. Kannis [g], S. Pütz [b,h], H. Sharma [b,c], V. Verhoeven [b,h]

[a] Institut für Kernphysik, Forschungszentrum Jülich, Wilhelm-Johnen-Straße, Jülich, 52428, NRW, Germany
[b] GSI, Helmholtzzentrum für Schwerionenforschung, Planckstraße 1, Darmstadt, 64291, Hessen, Germany
[c] FH Aachen - University of Applied Sciences, Bayernallee 11, Aachen, 52066, NRW, Germany
[d] European Organization for Nuclear Research, CERN, Esplanade des Particules 1, Geneva, 1211, Genf, Switzerland
[e] Istituto Nazionale di Fisica Nucleare, Laboratori Nazionali di Frascati, Via Enrico Fermi 54, Frascati, 00044, Rome, Italy
[f] III. Physikalisches Institut B, RWTH Aachen, Templergraben 55, Aachen, 52062, NRW, Germany
[g] Heinrich-Heine-Universität Düsseldorf, Universitätsstraße 1, Düsseldorf, 40225, NRW, Germany
[h] Universität zu Köln, Albertus-Magnus-Platz, Köln, 50923, NRW, Germany

ARTICLE INFO

Keywords:
Atomic beam source
Polarized target
Nuclear polarized hydrogen
LHCb
Hydrogen recombination
Interstellar medium

ABSTRACT

The LHC beams cannot be polarized. Hence, the implementation of a dense polarized gas target at the LHCb experiment at CERN, to be operated simultaneously with beam–beam collisions, will enable high-energy fixed target interactions to explore a range of spin physics measurements. Using an atomic beam source at the Forschungszentrum Jülich to provide a polarized atomic hydrogen beam, we investigated the properties of a storage cell coated with amorphous carbon. A notable recombination rate, lying between 93 and 100%, and a preservation of polarization during recombination exceeding 74% was observed. We were able to generate H_2 molecules with a nuclear polarization of −0.59. Remarkably, no water layer accumulated on the cooled storage cell surface, even over extended periods. Furthermore, we examined the influence of Lyman-α radiation on the recombination rate on carbon, addressing a prominent question in the field of astrophysics.

1. Introduction

Despite significant theoretical and experimental progress over the past decades, many fundamental aspects of the partonic structure of nucleons and nuclei remain poorly determined. Therefore, understanding the internal dynamical structure of protons and neutrons in terms of quarks and gluons remains one of the most important and pressing challenges of particle physics. The intrinsic complexity of the theory at the scale of confinement prevents precise predictions of even basic properties of the nucleons, such as their mass, radius, spin, and magnetic moment, solely based on first principles. Thus, an experimental approach is essential to advance our understanding of the nucleon structure and, more broadly, the strong force in this regime of QCD. Spin has emerged as a key tool for accessing this new domain.

Due to its particular forward geometry and capability to reconstruct collision events, especially those producing heavy flavor particles, with high accuracy, the LHCb experiment [1,2] at the Large Hadron Collider (LHC) at CERN is particularly suitable for integrating a polarized gas target system. In order to access the poorly explored kinematical range of the large negative Feynman x_F and the large Bjorken-x regions at intermediate Q^2 with beam–gas collisions at $\sqrt{s_{NN}} \sim 115$ GeV, the installation of a (transversely) polarized target is currently under study.

The already extensive list of potential discoveries and relevant measurements [3] derived from the use of the LHC proton beam will be further enriched by the unique opportunity to merge the LHC heavy-ion program with spin physics, enabling, for the first time, the study of polarized Pb-p$^{\uparrow\downarrow}$ and Pb-d$^{\uparrow\downarrow}$ collisions at GeV.

This R&D [4] poses its foundation on the recent deployment of the first ever installed unpolarized gaseous fixed-target system, SMOG2 [5], at LHC, placed in its primary vacuum sector, and upstream of the LHCb detector. The complete system was installed during the LHC Long Shutdown II, and has been running successfully since the beginning of LHC Run 3 (2022).

The LHCspin project aims to incorporate an atomic beam source along with a specialized T-shaped openable storage cell to deliver a dense, polarized atomic or molecular gas target to be traversed by the LHC beams, with a negligible impact on their lifetime.

* Corresponding author at: Institut für Kernphysik, Forschungszentrum Jülich, Wilhelm-Johnen-Straße, Jülich, 52428, NRW, Germany.
E-mail address: t.el-kordy@fz-juelich.de (T. El-Kordy).

https://doi.org/10.1016/j.nima.2024.169707
Received 20 June 2024; Received in revised form 29 July 2024; Accepted 3 August 2024
Available online 22 August 2024

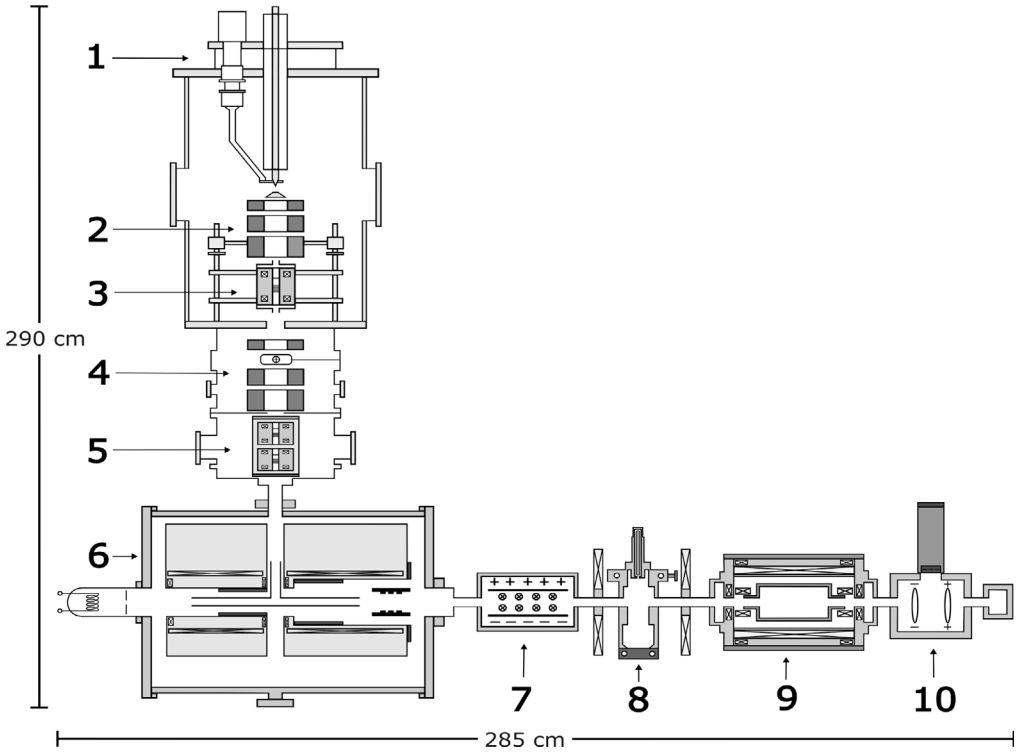

Fig. 1. Side view of ABS, Interaction chamber and LSP (1: Gas inlet, dissociator and nozzle cooling system, 2: Stern–Gerlach sextupole magnets, 3: MFT, 4: Second set of Stern Stern–Gerlach sextupoles with a beam chopper between the first and second magnet, 5: WFT and inactive strong field transition unit, 6: Interaction chamber with storage cell, superconducting solenoids, helium tanks and electron gun, 7: Wien filter, 8: Cesium cell, 9: Spinfilter, 10: Quench chamber with PMT and Faraday cup).

The openable cell, which consists of two halves that can be separated transversely with respect to the beam direction during the beam injection and tuning phases, allows the passage of the beam when its transverse size is much larger than the one during Lumi Runs operations. A safe diameter of 5 cm in the open position can be assumed when considering the critical scenario of colliding beams. However, for this R&D a cylindrical storage cell with a fixed inner diameter of 11 mm has been used.

In general, the characteristic behavior of the storage cell depends primarily on the inner surface coating, which needs to meet specific criteria for its suitability in subsequent use. Particularly, the preservation of polarization within the stored atomic gas is essential. Depending on the application, highly efficient atom recombination on the surface may be necessary or should be avoided entirely. Additionally, high vacuum compatibility, i.e. a low rate of outgassing, and low Secondary Electron Yield (SEY), are required. Specifically, these requirements prohibit the presence of a water–ice coating, as utilized at HERMES [6], which has thus far resulted in the highest level of polarization preservation. Materials exhibiting ferromagnetism must be circumvented, as magnetic field gradients on the surface lead to a rapid loss of polarization. Moreover, a high SEY could induce large instabilities on the accelerator beam and also create background to the spectrometer.

In this paper we investigate the possibility of employing a storage cell coated with amorphous carbon, as the one adopted for the SMOG2 storage cell, to serve as a source for a fixed polarized molecular hydrogen gas target. While earlier efforts to produce polarized hydrogen targets proved to be challenging [7], this goal can be accomplished using an atomic beam source (ABS), formerly employed for the ANKE (Apparatus for Studies of Nucleon and Kaon Ejectiles) spectrometer at COSY [8], along with an interaction chamber and an associated Lamb-shift polarimeter (LSP) [9]. The complete setup, shown in Fig. 1, enables the generation of nuclear polarized atomic and molecular hydrogen beams and facilitates subsequent measurements of their polarization and recombination rates, thereby allowing for the exploration of the properties of gas-storage cells.

Beyond accelerator physics, the study of hydrogen recombination on carbon surfaces holds significance due to an unresolved question in astrophysics. In the interstellar medium (ISM), hydrogen is the most prevalent element, often found initially in the form of atomic hydrogen clouds. Over time they transition to molecular hydrogen clouds, increasing in density. Nebulae can ultimately collapse to form stars, and as stars reach the end of their lifecycle, hydrogen clouds re-emerge, initiating the cycle once more. However, the process behind the formation of molecular hydrogen is not yet fully understood [10]. Within the ISM, surface catalyzed recombination on carbonaceous grains is a promising candidate in the search for an efficient mechanism of H_2 formation. In this paper we will discuss the effect of Lyman-α radiation on the recombination rate of chemisorbed hydrogen atoms on an amorphous carbon surface.

2. Setup

The present section focuses on the individual components contained within the ABS, interaction chamber, and LSP, alongside intricate pumping and cooling systems necessary to maintain a sufficiently high and stable vacuum, and to ensure the reliable operation of all components.

2.1. Atomic beam source

2.1.1. Dissociator and Stern–Gerlach sextupole magnets

Molecular hydrogen gas introduced into a borosilicate glass discharge tube at a flow rate of 1.1 $\frac{\text{mbar L}}{\text{s}}$, is dissociated primarily into ground-state ($1S_{1/2}$) atoms through the application of a 300 W coupled radio frequency at 13.56 MHz. The atomic hydrogen beam exits the dissociator discharge tube through a conical-shaped aluminum nozzle, cooled by a heat bridge linked to a coldhead operating with compressed helium gas. The nozzle's tip reaches a temperature of 70 K, aiding in optimizing the gas jet's passage through a stainless-steel

beam skimmer. The cooling process also reduces the particle velocity, thereby extending the time of flight through the subsequent sextupole Stern–Gerlach setup. Strong focusing and defocusing fields of the latter then enable a significant level of electron spin polarization.

Within the Paschen-Back region, the four hyperfine substates of ground-state hydrogen can be described using the uncoupled state $|n, m_S, m_I\rangle$, incorporating the principal quantum number n, electron spin projection m_S, and the nuclear spin projection m_I: $|1\rangle = |1, +\frac{1}{2}, +\frac{1}{2}\rangle$, $|2\rangle = |1, +\frac{1}{2}, -\frac{1}{2}\rangle$, $|3\rangle = |1, -\frac{1}{2}, -\frac{1}{2}\rangle$ and $|4\rangle = |1, -\frac{1}{2}, +\frac{1}{2}\rangle$. The radial force $\mathbf{F}_r$ exerted by an external magnetic field B on an atom with magnetic moment μ_{atom} is proportional to the distance r to the central axis of symmetry [8]: $\mathbf{F}_r = -\mu_{atom} \frac{dB}{dr} \frac{\mathbf{r}}{r}$. As μ_{atom} is dominated by the magnetic moment of the electron, we can employ the strong permanent Stern–Gerlach sextupole magnets to ensure a good spatial separation of the two electron spin-up substates $|1\rangle$ and $|2\rangle$ from the remaining ones.

2.1.2. Transition units

We utilize either a weak (WFT) or a medium field transition unit (MFT) to establish a specific hyperfine substate or combinations of them. These transition units consist of a small magnetic field gradient B_{grad} on top of a static homogeneous field B_{hom} in the Zeeman region, along with a radio frequency (RF) possessing a magnetic field component orthogonal to the static field. As atoms pass through the gradient, the energy difference between various hyperfine substates continuously varies. The RF is selected such that there is at least one point along the gradient where the energy difference between two substates matches the RF photon energy, enabling magnetic dipole transitions. As only two hyperfine substates are present among the incoming atoms, a change in the occupation number follows.

The total angular momentum operator $\vec{F}$ can be constructed by adding the nuclear spin operator $\vec{I}$ and the electron spin operator $\vec{S}$ as follows: $\vec{F} = \mathbb{1} \otimes \vec{S} + \vec{I} \otimes \mathbb{1}$. In the Zeeman region, the four hyperfine substates can be described by the coupled state $|F, m_F\rangle$, with total angular momentum quantum number F and its projection m_F: $|1\rangle = |1, +1\rangle$, $|2\rangle = |1, 0\rangle$, $|3\rangle = |1, -1\rangle$ and $|4\rangle = |0, 0\rangle$. The WFT takes advantage of the fact that, under weak magnetic field strengths, in our case $B_{grad} + B_{hom} \leq 1$ mT, the $F = 1$ substates $|1\rangle$, $|2\rangle$ and $|3\rangle$ display nearly equal spacing under the influence of the same external magnetic field. This condition enables the RF with 8.4 MHz to induce transitions, resulting in a complete repopulation from $|1\rangle$ to $|3\rangle$, with $|2\rangle$ serving only as an intermediate substate [11]. Transitions involving the change $|\Delta m_F = 2|$, on the other hand, are prohibited by the selection rules of angular momentum.

Unlike the WFT, the MFT operates at marginally higher magnetic field values, where the energy spacings between hyperfine states vary from one another for a given magnetic field strength. The RF with 59.5 MHz then facilitates sequential transitions: initially between $|1\rangle$ and $|2\rangle$ and subsequently from $|2\rangle$ to $|3\rangle$, resulting in a mixture of substates $|1\rangle$ and $|3\rangle$. In the ABS, the MFT works in combination with a second set of Stern–Gerlach sextupole magnets, utilized to defocus H atoms in substate $|3\rangle$ while focusing substate $|1\rangle$ on the beam line, thus allowing for a beam entirely in substate $|1\rangle$, or if the MFT gradient were to be reversed, entirely in substate $|2\rangle$.

The Breit-Rabi diagram in Fig. 2 illustrates the eigenenergies of the hyperfine substates at various magnetic field strengths, along with the transitions between them.

2.2. Interaction chamber

The interaction chamber houses the T-shaped storage cell, surrounded by two superconducting niobium–titanium solenoids. These magnets, cooled by thermally shielded liquid helium to reach the critical temperature of 5.4 K, are capable of generating a magnetic field of up to 1 T. The polarized ABS beam enters the interaction chamber from above and proceeds directly into the center of the chamber, where the storage cell, permanently maintained at a temperature of 100 K, is located. An electron gun on one side emits a beam of electrons with energies up to 150 eV into the storage cell. Cryogenic panels, composed of activated carbon, enhance the pumping power, enabling pressure levels in the range of 10^{-8} mbar.

The storage cell, crafted from fused quartz, possesses an inner diameter of 11 mm and a length of 400 mm. Upon entry, atoms collide with the inner surface of the storage cell, undergoing either elastic collisions or adsorbing to the surface before desorbing in a cosine distribution. As a result, the atoms are temporarily 'stored' within the cell, resulting in areal target densities of up to 10^{14} cm^{-2}. Depending on the surface material and the polarization of the beam, recombination back into H_2 can occur. The electron beam ionizes atoms and molecules within the cell and is capable of dissociating the molecules as well:

$$H + e^- \rightarrow H^+ + 2e^-, \quad H_2 + e^- \rightarrow H_2^+ + e^-, \quad H_2 + e^- \rightarrow H + H^+ + 2e^- \quad (1)$$

An electric potential of 1.5 kV along the storage cell accelerates ions out of the cell and into the LSP. We coated the inner surface with a 200 nm thick layer of amorphous carbon, chosen partially for its low SEY (see Section 3). Furthermore, this surface's conductivity effectively prevents the buildup of localized charges that might otherwise deflect the accelerator beam.

2.3. Lamb-shift polarimeter

2.3.1. Wien filter

The acceleration of particles with different masses by the same potential allows the Wien filter to function as a mass spectrometer. A configuration of a perpendicular electric and magnetic field is utilized, ensuring that particles with the specified mass remain unaffected while others are deflected.

The acceleration potential U (in V) required to filter a particle of mass m (in kg) relies on the charge q (in C) of the particle, as well as the strength of the applied electric field E (in $\frac{\mathrm{V}}{\mathrm{m}}$) and magnetic field B (in T), expressed by

$$U(m) = \frac{m}{2q} \left(\frac{E}{B} \right)^2 . \quad (2)$$

2.3.2. Cesium cell

Protons or H_2^+ ions traverse a cell where cesium from a fractured glass ampule is evaporated by two heating elements, creating a constant gas flow in the beamline through a temperature gradient. A charge exchange reaction between the Cs vapor and the ion beam partially leads to the creation of metastable atomic hydrogen atoms through the reactions $Cs + H^+ \rightarrow Cs^+ + H_{2S_{1/2}}$ or $Cs + H_2^+ \rightarrow Cs^+ + H_{2S_{1/2}} + H$. A set of cylindrical coils, supplied with 15 A, is positioned in front and behind the cesium cell to maintain a continuous quantization axis at around 50 mT to retain polarization. Metastable hydrogen also possesses four hyperfine substates, denoted as $|\alpha_1\rangle$, $|\alpha_2\rangle$, $|\beta_3\rangle$ and $|\beta_4\rangle$. With a critical magnetic field of 6.35 mT, metastable hydrogen lies well within the Paschen-Back region during the charge exchange, and can be described using the uncoupled basis $|n, m_S, m_I\rangle$: $|\alpha_1\rangle = |2, +\frac{1}{2}, +\frac{1}{2}\rangle$, $|\alpha_2\rangle = |2, +\frac{1}{2}, -\frac{1}{2}\rangle$, $|\beta_3\rangle = |2, -\frac{1}{2}, -\frac{1}{2}\rangle$ and $|\beta_4\rangle = |2, -\frac{1}{2}, +\frac{1}{2}\rangle$. For this reason, the polarized proton or H_2^+ beam entering the cesium cell will result in either a beam containing $|\alpha_1\rangle$ and $|\beta_4\rangle$ (both with proton spin $+\frac{1}{2}$), or a beam containing $|\alpha_2\rangle$ and $|\beta_3\rangle$ substates (proton spin $-\frac{1}{2}$).

2.3.3. Spinfilter

The spinfilter consists of a cavity that incorporates a coupled RF with 1.609 GHz, alongside a static transversal electric field of 10 $\frac{\mathrm{V}}{\mathrm{cm}}$ and a homogeneous longitudinal magnetic field set to either 53.5 mT or 60.5 mT. Its functionality lies in permitting the transmission of either the $|\alpha_1\rangle$ or $|\alpha_2\rangle$ hyperfine substate of metastable hydrogen atoms while simultaneously quenching all other substates, causing them to transition into the ground state [12,13].

The electric field is employed to reduce the lifetime of the $2S_{1/2}$ atoms by facilitating transitions into the $2P_{1/2}$ substates, which promptly

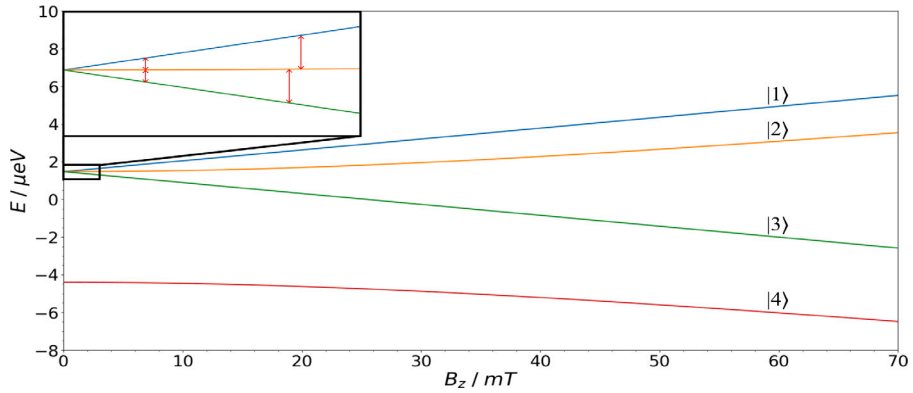

Fig. 2. The Breit-Rabi diagram for the ground state of hydrogen displays the eigenenergies E for all hyperfine substates as a function of the applied magnetic field B_z. The inset provides a visualization of the potential weak-field and medium-field transitions. For small magnetic fields, the energy difference between hyperfine substates $|1\rangle$ and $|2\rangle$, as well as between $|2\rangle$ and $|3\rangle$, is nearly equal.

result in a decay to the ground state. The RF induces transitions between hyperfine substates by delivering photons with energy equivalent to the energy difference between them. This energy difference depends on the external magnetic field being applied [14].

2.3.4. Quenching chamber

A strong electric field in the quenching chamber forces the remaining metastable atoms behind the spinfilter to undergo a decay into the ground state (Stark effect). This process results in the emission of Lyman-α photons, detectable by a photomultiplier and enables the determination of polarization. Moreover, a Faraday cup, located along the beam axis at the rear of the quenching chamber can measure the ion intensity in the beam.

3. Storage cell coating

The emission of secondary electrons from carbon materials is highly dependent on their allotropic form. Diamond (sp^3 hybridization) exhibits a maximum SEY above 10 [15], whereas graphite (sp^2 hybridization) has a maximum SEY approaching 1 [16]. Consequently, amorphous carbon thin films, typically comprising a mix of sp^3 and sp^2 hybridized domains [17], can exhibit a wide range of SEY values [18].

To produce films with a maximal SEY below the threshold for electron multipacting in particle accelerators (typically between 1.1 and 1.4 [19–21]), the deposition process must favor the formation of sp^2 carbon–carbon bonding. This can be achieved by sputtering carbon atoms from a graphite target and limiting the incorporation of hydrogen impurities [22]. A measurement of the SEY spectrum of a carbon film deposited on a witness sample revealed a maximal SEY of 1.24 at 250 eV, as shown in Fig. 3. A miniaturized magnetron sputtering source was developed to coat the inner walls of the quartz storage cell (Fig. 4). The graphite target, with a diameter of 2 mm and a length of 20 mm (ash content below 200 ppm), and the stainless-steel anodes are mounted on a copper cylinder that centers the assembly inside the storage cell. A Kapton-insulated cable supplies DC voltage to the target and allows the sputtering source to be moved along the 400 mm length of the storage cell during the deposition process, ensuring full coverage, including two 50 mm extensions at each end (Fig. 4(a) and (b)). The deposition process occurs inside an ultra-high vacuum (UHV) chamber, within a magnetic field of 50 mT provided by an external solenoid with field lines parallel to the target surface. Before deposition, the system is vacuum-pumped and baked for 24 hours at 150 °C, achieving a base pressure of $2 \cdot 10^{-9}$ mbar after cooling to room temperature. Argon with purity 6.0, at a pressure of $4 \cdot 10^{-1}$ mbar, is used as the discharge gas. At a constant power of approximately 4 W (U = 710 V, I = 5 mA), it takes 40 hours to coat the entire cell with a thickness of about 200 nm. Fig. 4(c) shows the sputtering source in operation. To reduce hydrogen partial pressure during the deposition process, an additional target intermittently deposits a getter material (Ti–Zr–V) on portions of the vacuum chamber walls.

4. Molecular polarization and recombination

When two hydrogen atoms form a covalent bond, the two electrons of the resulting H_2 molecule are required to have antiparallel spins as a consequence of the Pauli exclusion principle. In contrast, the protons constituting the atomic nuclei can couple their spins, leading to the categorization of H_2 into ortho-hydrogen with a total nuclear spin $I = 1$ and para-hydrogen with $I = 0$. Ortho-hydrogen can only possess rotational wavefunctions that are antisymmetric with respect to the exchange of both protons. Consequently, the rotational quantum number J is limited to odd values. Conversely, para-hydrogen permits only even J values, as its rotational wavefunctions must be symmetric under the exchange of both protons. Considering the spin projection M_I, ortho-hydrogen forms a triplet state $|I, M_I\rangle = |1,+1\rangle, |1,0\rangle, |1,-1\rangle$, while para-hydrogen only has a singlet state $|I, M_I\rangle = |0,0\rangle$.

The recombination of two hydrogen atoms in hyperfine substates $|1\rangle$ or $|3\rangle$ results in a molecular polarization in the ortho-hydrogen basis state $|1,+1\rangle$ or $|1,-1\rangle$, respectively, corresponding to both nuclear spins being up or down. At low temperatures ($< 200\ K$), only the $J = 1$ molecular rotational state is populated, known to have a critical magnetic field of $B_{c,m} = 5.4$ mT [23]. Generally, the molecular polarization is constrained by the atomic polarization. From there, a polarization loss can occur during the recombination process itself and afterward due to collisions with the storage cell's inner surface. In [23] Wise et al. provide a formula describing the molecular polarization P_m after n wall collisions in an external magnetic field B:

$$P_m(B,n) = P_{m0}\, e^{-n\left(\frac{B_{c,m}}{B}\right)^2}, \tag{3}$$

where P_{m0} is the molecular polarization right after recombination. The distribution of the number of wall collisions can be described by the probability density function of an exponential distribution

$$W(n) = \alpha\, e^{-\alpha n}, \tag{4}$$

where α is a parameter, which depends on the geometry and surface material of the storage cell [24,25]. Using the mean value $\tilde{n} = \frac{ln(2)}{\alpha}$ of Eq. (4), the weighted average

$$\bar{P}_m(B) = \int_0^{+\infty} P_m(B,n) W(n)\, dn = \frac{\alpha P_{m0}}{\alpha + \left(\frac{B_{c,m}}{B}\right)^2} \tag{5}$$

can be expressed as:

$$\bar{P}_m(B) = \frac{P_{m0}}{1 + \frac{\tilde{n}}{ln(2)}\left(\frac{B_{c,m}}{B}\right)^2}. \tag{6}$$

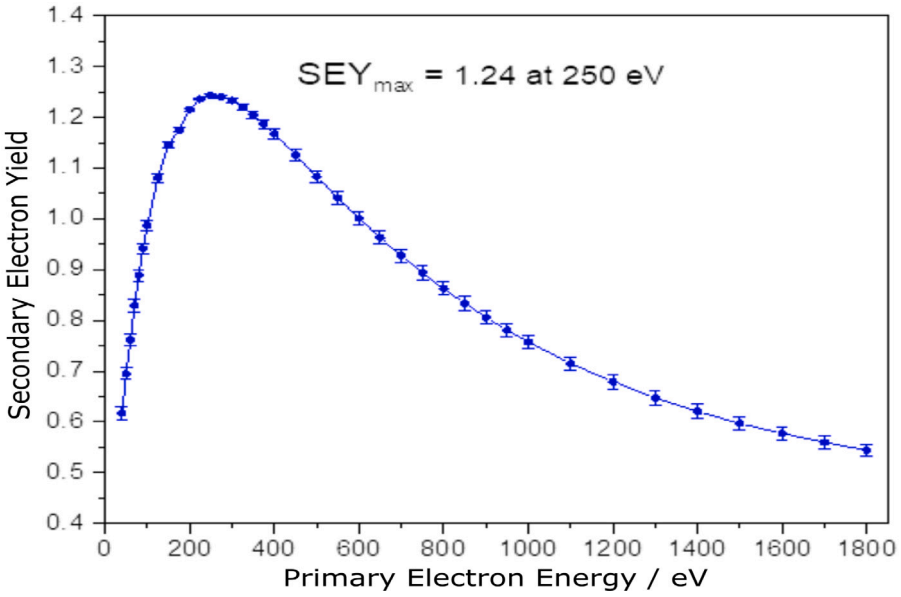

Fig. 3. The SEY spectrum of the carbon film deposited on a witness sample placed in one of the 50 mm extensions.

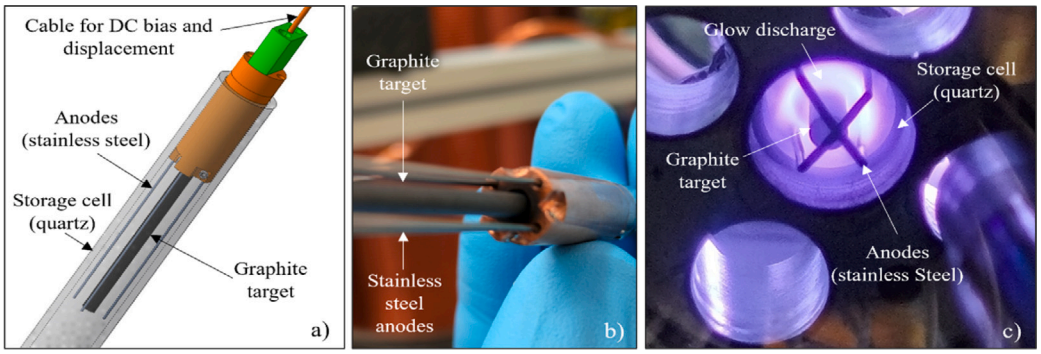

Fig. 4. (a) Drawing of the miniaturized sputtering source inside the quartz storage cell. (b) The graphite target (cathode) and the stainless-steel anodes mounted on the copper holder that centers the assembly. (c) The magnetron sputtering source in operation utilizes argon as the discharge gas to deposit carbon atoms from a graphite target onto the storage cell substrate.

The number of wall collisions varies considerably depending on the material. It was demonstrated that elastic scattering on the surface corresponds to a mean value of $\tilde{n} = 120 \pm 10$ [26]. However, when particles undergo adsorption and subsequent desorption from the surface, the sharper angular distribution, described by a cos or $\cos^2$ relation, increases the mean value to $\tilde{n} \sim 300$ or even higher.

Polarization losses occur as the projection M_J of the rotational state can change after each wall collision, potentially affecting the nuclear spin due to its coupling to the molecular rotation. The use of a strong external magnetic field $B \gg B_{c,m}$ can prevent depopulation caused by this effect, as well as polarization loss due to electron–proton coupling within the hydrogen atoms. Polarization losses resulting from the coupling of both nuclear spins to each other may be neglected. The proton polarization can therefore be expressed as

$$P_p(B) = aP_a + b\bar{P}_m = aP_a + \frac{bP_{m0}}{1 + \frac{\tilde{n}}{ln(2)}\left(\frac{B_{c,m}}{B}\right)^2}, \tag{7}$$

where P_a is the polarization of the atomic hydrogen beam originating from the ABS, a is the fraction of protons resulting from ionized H atoms and $b = 1 - a$ is the fraction of protons arising from H_2 molecules. Previously, polarizations of up to $P_a = 0.9$ were achieved. If the hydrogen atoms are polarized in $|1\rangle$ or $|3\rangle$, the polarization of the nucleus will be preserved even after ionization in a weak external magnetic field, contrary to the behavior observed for polarized H_2.

The recombination rate c describes the number of recombinations per pair of hydrogen atoms. It is convenient to determine c by examining the proton fractions:

$$c = \frac{2b}{ak + 2b}. \tag{8}$$

The factor k is defined as the ratio between the cross section for dissociation of H_2 via electron impact and the cross section for the ionization of a hydrogen atom by electron impact: $k = \frac{\sigma(H_2 \to H^+ + H)}{\sigma(H \to H^+)} = 0.18$. It represents the relative likelihood of a proton originating from H_2 compared to H.

Hydrogen atoms possessing both electron and nuclear polarization cannot undergo direct recombination due to the requirement of electrons having opposite spins. Nevertheless, recombination can take place through various surface-catalyzed mechanisms, including the Langmuir-Hinshelwood mechanism, the Eley-Rideal mechanism, the hot-atom mechanism, and radiation-induced desorption [27]. These processes determine the initial polarization P_{m0} of the molecules.

Previous measurements conducted at the ANKE ABS revealed consistently low recombination rates in storage cells that were coated with aluminum or Teflon [28]. In a vacuum, cold surfaces tend to capture water from the residual gas, resulting in the formation of a water layer on the surface of the storage cell. This layer has been proven to effectively prevent any recombination from taking place [29]. In contrast, Wise et al. demonstrated a recombination rate exceeding 0.85

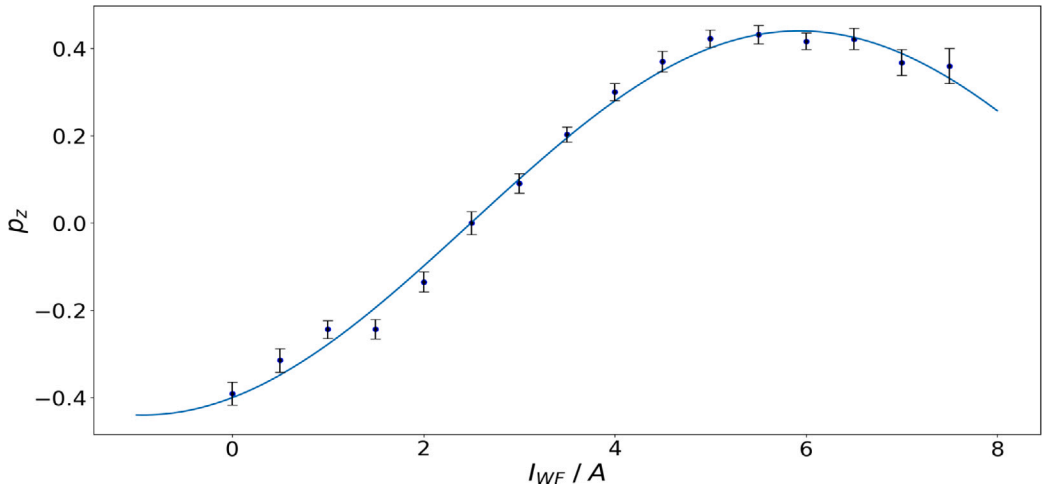

Fig. 5. The proton vector polarization p_z varies with the current I_{WF} applied to the Wien filter for establishing a magnetic field. A fit to the data yields $p_0 = 0.44 \pm 0.01$, $n = 0.46 \pm 0.01$ A^{-1} and $m = 3.57 \pm 0.04$.

on a cell surface lined with a copper mesh, aimed at increasing the number of wall collisions. Gold surfaces exhibit a recombination rate close to 1 within a temperature range of 45 to 100 K [30]. Similarly, surfaces coated with perfluoropolyether, commonly referred to as Fomblin, exhibited a recombination rate close to 1 as well [25,31]. In case of carbon surfaces, it was proposed that recombination can only occur via radiation induced desorption, a process where neighboring atoms on a surface can recombine when radiation breaks their surface bond.

On gold and copper surfaces, the preservation of polarization during recombination is restricted to 50%. This limitation arises because all atoms adsorbed to the metal surface lose their nuclear polarization owing to strong relaxation processes. Only the atom acquired from the gas phase for recombination retains its polarization. Fomblin, on the other hand, fully preserves polarization throughout recombination. However, it tends to rapidly accumulate a water layer due to its polar surface. Additionally, being an oil, it is unsuitable for vacuum applications, despite its high vapor pressure, which falls within the range of 10^{-7} mbar.

5. Results and analysis

5.1. Wien filter curve

The Larmor precession of the proton is characterized by an angular frequency, $\omega_L = -\gamma B$, where $\gamma = g_p \frac{e}{2m_p}$ represents the particle-specific gyromagnetic ratio, dependent on the particle's mass m_p, charge e, and proton g-factor $g_p = 5.58$ [32], while B denotes the magnitude of the external magnetic field. The angle covered over time τ is thus $\beta_L = \omega_L \tau$. Upon entry into the Wien filter, the proton's magnetic moment no longer aligns with the external field lines since the Wien filter possesses a magnetic field perpendicular to the previous quantization axis, which was along the beam direction. In contrast to the strong spin magnetic moment of the unpaired electron in the H_2^+ molecular ion, which follows changes adiabatically due to the small relative change of the magnetic field compared to its Larmor frequency ($\frac{dB}{dt} \ll \omega_L$), the proton's magnetic moment gradually adjusts its orientation while passing through the Wien filter.

Depending on the field strength, particle velocity v_p, and time spent in the Wien filter, protons may undergo a 180° flip in orientation relative to their original alignment due to insufficient time to align completely with the perpendicular field lines. Identifying the magnetic field strength for such a flip is critical, as any deviation from the initial quantization axis would lead to polarization loss once the protons exit the spinfilter and return to the previous magnetic field. The required field strength, given the length of the Wien filter l_{WF} and proton energy E_p, is determined by

$$\beta_L = \omega_L \tau = -\gamma B \frac{l_{WF}}{v_p} = -\gamma B \frac{l_{WF}}{\sqrt{\frac{2E_p}{m_p}}} = \pi \text{ rad.} \tag{9}$$

Fig. 5 depicts a measurement of the vector polarization p_z of a proton beam based on the applied current I_{WF}, which is proportional to the magnetic field strength. The resulting curve can be fitted by a cosine function:

$$p_z(I_{WF}) = p_0 \, cos(n \, I_{WF} + m), \tag{10}$$

where p_0 represents the initial proton polarization, n is a scaling factor, and m is the phase. The associated error bars arise from background noise within the PMT signal, thereby introducing uncertainty into the Gaussian fit of the measured peaks.

These findings facilitate the minimization of polarization losses in the Wien filter for subsequent polarization measurements of atomic beams, by deliberately choosing the current to introduce a flip in the spin projection. The polarization of protons in the H_2^+ molecular ions remains unaffected by the Wien filter magnetic field, as their total angular momentum follows magnetic field changes adiabatically due to the large magnetic moment of the unpaired electron.

5.2. Polarization measurements

Utilizing the MFT in combination with Stern–Gerlach magnets enables the polarization of atoms in the substate $|1\rangle$. Following ionization of the atoms, in case no recombination occurred beforehand, polarized protons proceed through the Wien filter, where any other ions are removed from the beam. Within the cesium cell, metastable substates $|\alpha_1\rangle$ and $|\beta_4\rangle$ are formed, with $|\beta_4\rangle$ subsequently being removed in the spinfilter. Ramping the spinfilter magnetic field produces a spectrum containing the $|\alpha_1\rangle$-peak with amplitude N_1 and the $|\alpha_2\rangle$-peak with amplitude N_2, allowing for the derivation of vector polarization: $p_z = \frac{N_1 - N_2}{N_1 + N_2}$ [33].

Using the MFT, the highest level of $|\alpha_1\rangle$-polarization we attained was $p_z = 0.42 \pm 0.03$. The corresponding spectrum is shown in Fig. 6. Employing the WFT enables the establishment of polarization in the $|\alpha_2\rangle$ substate following a similar process. We achieved a maximum vector polarization of $p_z = -0.64 \pm 0.02$ for an atomic beam, as depicted in Fig. 7.

Configuring the Wien filter to selectively filter H_2^+ ions, primarily originating from the ionization of recombined H_2, allows us to assess the nuclear polarization of the recombined molecules. Although the

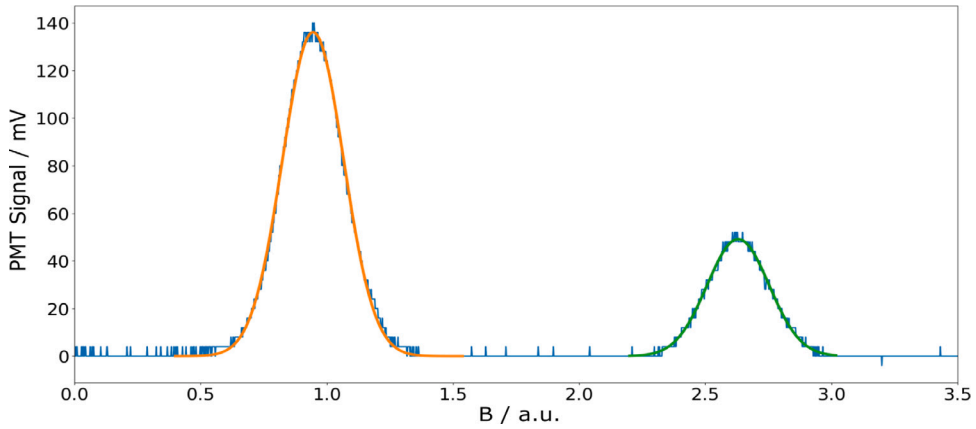

Fig. 6. The polarization spectrum of the LSP, generated by ramping the magnetic field of the spinfilter over time, depicts the $|\alpha_1\rangle$-peak (left) and $|\alpha_2\rangle$-peak (right), along with an associated Gaussian fit. Utilizing the MFT, a vector polarization of $p_z = 0.42 \pm 0.03$ was achieved for a $2S_{1/2}$ atomic hydrogen beam.

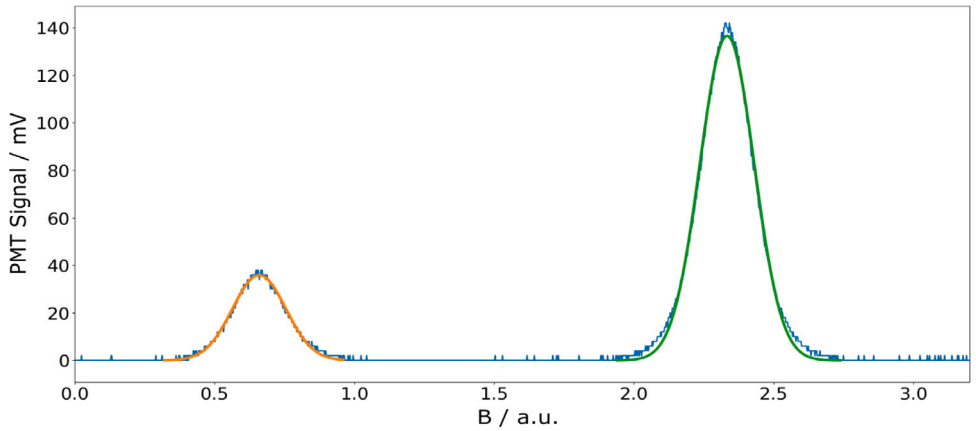

Fig. 7. The polarization spectrum, acquired by the WFT, for a $2S_{1/2}$ atomic hydrogen beam polarized in the $|\alpha_2\rangle$ substate demonstrates a vector polarization of $p_z = -0.64 \pm 0.02$.

polarization cannot be directly measured, a small fraction of the H_2^+ ions entering the cesium cell undergo charge exchange reactions with the cesium atoms, yielding metastable hydrogen atoms. Under the condition of sufficiently strong external magnetic fields, no substantial loss of nuclear polarization is anticipated during this process. However, upon transitioning to molecular measurements, the beam intensity notably decreased by a factor of 35 ± 5.

As depicted in Fig. 8, a molecular nuclear polarization of $p_z = -0.59 \pm 0.02$ was achievable. Based on earlier measurements, an initial atomic polarization of 0.8 upon entry of the hydrogen atoms into the storage cell can be assumed, thereby implying a polarization preservation of approximately 74%. Roughly 3.5% of particles entering the storage cell consist of unpolarized hydrogen molecules. These molecules either traversed the ABS without initial dissociation or passed through after recombining again in the dissociator [25]. Factoring this in, the actual preservation of polarization arguably surpasses 74%. The precise determination, however, is challenging as the ratio of unpolarized H_2 in the molecular LSP-beam depends on the recombination rate. In case of minimal recombination for instance, the constant fraction of initially unpolarized H_2 will be a significant contributor alongside the fraction of depolarized H_2. Since these measurements were conducted with a 300 mT field applied in the storage cell, polarization losses due to wall collisions are not expected to occur.

Deducing the recombination rate by comparing beam intensity for protons and H_2^+ ions is imprecise due to distinct ion types experiencing different focusing. Hence, it is more convenient to analyze the proton beam alone. With Eq. (7) the distinct proton fractions a and b, corresponding to atomic and molecular origins, can be determined. By measuring the proton polarization established by the WFT across various superconductor magnetic field strengths in an interval from 91 to 527 mT, a fit of Eq. (7) to the experimental data can reveal the influence of the amorphous carbon coating on the recombination rate.

As shown in Fig. 9, the absolute value of proton polarization reaches saturation for external magnetic fields on the order of a few hundred milliteslas. That means, the magnetic field's strength is sufficient to uncouple the nuclear spin from the molecular rotational angular momentum, preventing wall collisions from altering the proton spins within the H_2 molecule. Taking the observed molecular vector polarization of -0.59 ± 0.02 as saturated polarization value for H_2 molecules originating from the storage cell, along with the initial atomic polarization of 0.8, only the parameters n and a remain to be fitted. The fraction a is limited to the interval $[0, 1]$ and the number of wall collisions n is confined to positive integers. The fitted parameters are then determined as $a = 0.16 \pm 0.18$ and $n = 400 \pm 300$. Using Eq. (8), the recombination rate consequently falls between 93% and 100%. The calculated uncertainties in the measurement in Fig. 9 stems from background noise within the PMT signal and small inhomogeneities in the magnetic field of the spinfilter, resulting in a more efficient filtering of the $|\alpha_1\rangle$ substate compared to $|\alpha_2\rangle$.

5.3. Recombination measurements

In diffuse clouds, direct recombination via photon emission in a cold gas phase, as outlined by Gould and Salpeter in [34], is insufficient to explain the abundance of molecular hydrogen, as ultraviolet radiation continuously dissociates molecules [35]. Furthermore, the low densities

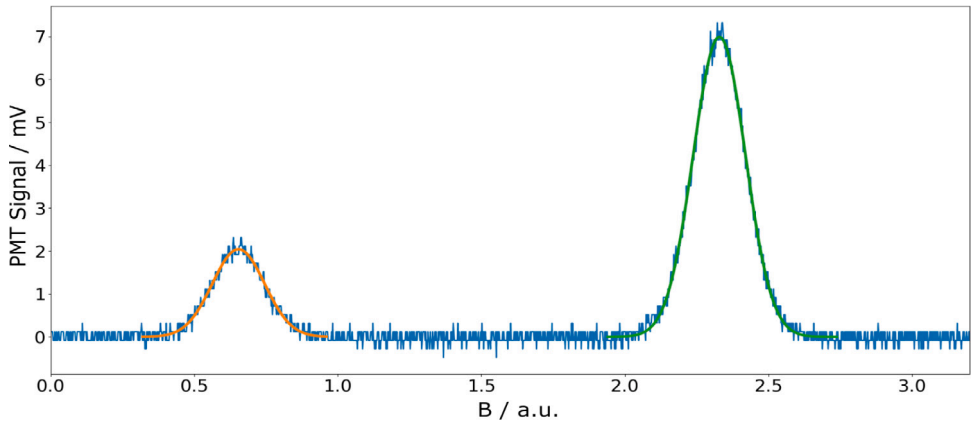

Fig. 8. For a nuclear-polarized molecular hydrogen beam, the polarization spectrum obtained by a WFT reveals a vector polarization of -0.59 ± 0.02.

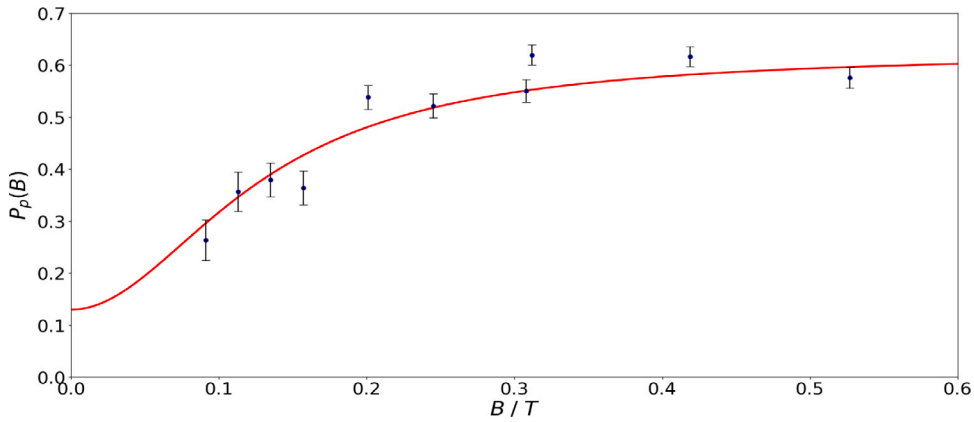

Fig. 9. The absolute value of the proton vector polarization is depicted for various superconductor magnetic fields, along with the corresponding fit-function. The function considers an initial atomic beam polarization of $P_a = 0.8$ and an initial molecular polarization of $P_{m0} = 0.59$.

make three-particle interactions improbable, which lead to the well-established conclusion that catalyzed recombinations occurring on the surfaces of dust grains in the interstellar medium are the primary source of molecular hydrogen [36]. These grains are classified based on their composition as silicates, carbonaceous solids and grains covered with water ice, albeit their precise composition remains largely unknown [27]. In the past, numerous experiments have been conducted on graphite surfaces, which serve as idealized representations of dust grains [37,38]. On the other hand, research on amorphous carbon surfaces has been notably limited.

At grain temperatures in the range of 100 K, the presence of physiosorbed atoms on the surface becomes untenable, rendering the Langmuir-Hinshelwood mechanism ineffective. Consequently, only chemisorbed atoms can persist on the surface, necessitating alternative recombination mechanisms. In Ref. [39], Casolo et al. investigated the recombination of chemisorbed hydrogen atoms via the Eley-Rideal mechanism on graphite. Frigge explored the desorption of H_2 from a highly oriented pyrolytic graphite surface saturated with chemisorbed hydrogen atoms, induced by a 30 fs laser pulse with 400 nm wavelength [40]. Additionally, Alata et al. [41] demonstrated that vacuum ultraviolet irradiation of hydrogenated amorphous carbons effectively facilitates the formation of H_2.

In the dissociator, Lyman-α photons are continuously generated and can traverse the ABS to reach the storage cell. This enables us to observe its influence on the recombination rate of chemisorbed hydrogen atoms on an amorphous carbon surface saturated with H atoms. Lyman-α radiation, ubiquitous in the ISM, possesses a wavelength of 121.567 nm, corresponding to 10.2 eV. It is sufficient to break the C-H bond, with a bond energy of about 4.3 eV, allowing for radiation-induced recombination of hydrogen. To assess its effect, we installed a stainless-steel beam chopper between the first and second sextupole magnet of the second Stern–Gerlach setup, as illustrated in Fig. 1. Controlled by a stepper motor, the cylindrical device can be adjusted in three distinct orientations with respect to the ABS beam, allowing the beam to pass through unimpeded, stopping only particles along the central beam axis, or blocking the entire beam. In the partially closed position, the majority of hydrogen atoms can still pass through to reach the storage cell, while at least 90% of all Lyman-α photons are intercepted.

Nonetheless, our measurements did not provide conclusive evidence for the reduced radiation intensity affecting the recombination rate. It is conceivable that the photon intensity did not fall below the threshold required to provide a sufficient number of photons for all atoms to recombine. However, it should be highlighted that the recombination rate did not progressively decrease over the course of several weeks, as would be expected if a water layer started to accumulate on the storage cell coating. This behavior is unexpected and has not been observed for any other coating investigated previously, all of which necessitated regular heating to remove any water residues.

6. Conclusion

With the apparatus presented in this paper we conducted an investigation into the properties of a storage cell coated with a 200 nm amorphous carbon layer at the IKP Jülich. An atomic beam source was utilized to successfully generate an atomic ground-state hydrogen beam polarized in a specified hyperfine substate. A storage cell then facilitated an efficient surface-catalyzed recombination to H_2, achieving a recombination rate between 93% and 100% with the carbon coating. The majority of polarization was retained throughout and

after the recombination process. The presence of sufficiently strong external magnetic fields ensured the preservation of polarization, despite hundreds of wall collisions. During recombination, however, the preservation of > 74% of the initial atomic polarization indicates that nuclear polarization can be maintained while residing on the carbon surface. It was highly advantageous that, during several weeks of measurements, no disruptive water layer accumulated on the cooled carbon surface. Direct measurements in the Lamb-shift polarimeter yielded a proton polarization of -0.64 ± 0.02, while molecular polarization values of -0.59 ± 0.02 were attained. These findings demonstrate the feasibility of carbon coatings being used in storage cell development for the LHCspin project, provided sufficiently strong magnetic fields are applied, thereby offering a promising solution for a polarized molecular gas target to be installed at the LHCb experiment along LHC at CERN.

CRediT authorship contribution statement

T. El-Kordy: Writing – review & editing, Writing – original draft, Visualization, Supervision, Project administration, Methodology, Investigation, Formal analysis, Data curation, Conceptualization. **P. Costa Pinto:** Writing – review & editing, Writing – original draft, Visualization. **P. Di Nezza:** Writing – review & editing, Writing – original draft. **R. Engels:** Writing – review & editing, Validation, Supervision, Project administration, Methodology, Investigation. **M. Ferro-Luzzi:** Writing – review & editing, Project administration. **N. Faatz:** Writing – review & editing, Investigation. **K. Grigoryev:** Project administration, Investigation. **C. Kannis:** Writing – review & editing, Methodology, Investigation. **S. Pütz:** Investigation. **H. Sharma:** Writing – review & editing. **V. Verhoeven:** Writing – review & editing, Investigation.

Declaration of competing interest

The authors declare that they have no known competing financial interests or personal relationships that could have appeared to influence the work reported in this paper.

Data availability

Data will be made available on request.

Acknowledgments

C. Kannis was funded by the Deutsche Forschungsgemeinschaft (DFG, German Research Foundation) – 533904660. The authors would like to thank Bernard Henrist and Spyridon Fiotakis for the conception and construction of the miniaturized sputtering source, Yorick Delaup for the deposition process, and Marcel Himmerlich for the measurement of the SEY. Additionally, the corresponding author would like to extend his gratitude to Prof. Zacharias (Universität Münster) for the fruitful discussions on recombination.

References

[1] LHCb Collaboration, A.A. Alves Jr., et al., The LHCb detector at the LHC, JINST 3 (2008) S08005.
[2] LHCb Collaboration, R. Aaij, et al., LHCb detector performance, Internat. J. Modern Phys. A 30 (2015) 1530022.
[3] P. Di Nezza, et al., 25th International Symposium on Spin Physics (SPIN2023), PoS, Durham, NC, USA, 2024.
[4] LHCSpin, C.A. Aidala, et al., The lhcspin project, 2019, arXiv:1901.08002.
[5] LHCb Collaboration, LHCb SMOG upgrade, CERN-LHCC-2019-005, LHCB-TDR-020, 2019.
[6] C. Baumgarten, et al., Measurements of atomic recombination in the HERMES polarized hydrogen and deuterium storage cell target, Nucl. Instrum. Methods Phys. Res. A 496 (2003) 263–276.
[7] B. Goel, W. Heeringa, Spin polarized ICF targets, Nucl. Fusion 28 (1988) 355.
[8] M. Mikirtychyants, et al., The polarized H and D atomic beam source for ANKE at COSY-Jülich, Nucl. Instrum. Methods Phys. Res. A 721 (2013) 83–98.
[9] R. Engels, et al., Production of HD molecules in definite hyperfine substates, Phys. Rev. Lett. 124 (2020) 113003.
[10] S. Cazaux, A.G.G.M. Tielens, Molecular hydrogen formation in the interstellar medium, Astrophys. J. 575 (2002) L29–L32.
[11] J.P.M. Beijers, Adiabatic spin transitions in polarized-proton sources, Nucl. Instrum. Methods Phys. Res. A 536 (2005) 282–288.
[12] G.P. Lawrence, et al., Source of polarized negative hydrogen and deuterium ions, Phys. Lett. 28 (1969) 594–596.
[13] A.J. Mendez, et al., Installation of an on-line lamb shift spin-filter polarimeter in the triangle universities nuclear laboratory atomic beam polarized ion source, Rev. Sci. Instrum. 67 (1996) 3073–3081.
[14] R. Engels, et al., Precision lamb-shift polarimeter for polarized atomic and ion beams, Rev. Sci. Instrum. 74 (2003) 4607–4615.
[15] J. Cazaux, et al., About the secondary electron emission yield, δ, from e^--irradiated insulators, Mikrochim. Acta 132 (2000) 173–177.
[16] N. Rey Whetten, Secondary electron emission of pyrolytic graphite cleaved in a high vacuum, J. Appl. Phys. 34 (1963) 771–773.
[17] J. Roberston, Diamond-like amorphous carbon, Mater. Sci. Eng. R Rep. 37 (2002) 129–281.
[18] N. Bundaleski, et al., The role of hydrogen incorporation into Amorphous carbon films in the change of the secondary electron yield, Int. J. Mol. Sci. 24 (16) (2023) 12999.
[19] C. Yin Vallgren, et al., Amorphous carbon coatings for the mitigation of electron cloud in the CERN super proton synchrotron, Phys. Rev. ST Accel. Beams 14 (2011) 071001.
[20] V. Baglin, et al., Vacuum System, in: CERN Yellow Reports: Monographs, vol. 10, 2020, pp. 229–244.
[21] S. Verdu-Anders, et al., A beam screen to prepare the RHIC vacuum chamber for EIC hadron beams: Conceptual design and requirements, in: 12th Int. Particle Acc. Conf., IPAC2021, JACoW Publishing, Campinas, SP, Brazil, 2021, TUPAB260.
[22] C.F. Adame, et al., Amorphous carbon thin films: Mechanisms of hydrogen incorporation during magnetron sputtering and consequences for the secondary electron emission, Vac. Sci. Technol. A 41 (2023) 043412.
[23] T. Wise, et al., Nuclear polarization of hydrogen molecules from recombination of polarized atoms, Phys. Rev. Lett. 87 (2001) 042701.
[24] R. Engels, et al., Polarized molecules: A new option for internal storage-cell targets? in: XVIth International Workshop in Polarized Sources, Targets, and Polarimetry (PSTP2015) - Polarized Targets, PoS, Ruhr-University Bochum, Bochum, NRW, Germany, 2016, p. 008.
[25] R. Engels, et al., Production of hyperpolarized H_2 molecules from $\vec{H}$ atoms in gas-storage cells, Phys. Rev. Lett. 115 (2015) 113007.
[26] R. Engels, et al., Production and storage of polarized H_2, D_2 and HD molecules, in: XVII International Workshop on Polarized Sources, Targets & Polarimetry (PSTP2017), PoS, Kaist, Daejeon, South Korea, 2018, p. 033.
[27] V.and others Wakelam, H_2 Formation on interstellar dust grains: The viewpoints of theory, experiments, models and observations, Mol. Astrophys. 9 (2017) 1–36.
[28] K. Grigoryev, et al., The polarized internal gas target of anke at COSY, Int. J. Mod. Phys. E 18 (2009) 511–517.
[29] P. Lenisa, et al., Nuclear polarization of molecular hydrogen recombined on a non-metallic surface, Eur. Phys. J. D 29 (2004) 21–26.
[30] R. Engels, et al., IKP annual report 2011, 2011, Juel4349.
[31] R. Engels, et al., Polarized H_2, D_2 and HD molecules and their possible use to feed a polarized H_2^+, D_2^+ or HD^+ ion source for stripping injection into storage rings, in: Proceedings of the 24th International Spin Symposium (SPIN2021), JPS Conf. Proc. Matsue, Shimane Prefecture, Japan, 2022, 37021202.
[32] C. Smorra, A. Mooser, Precision measurements of the fundamental properties of the proton and antiproton, J. Phys.: Conf. Ser. (2020) 1412032001.
[33] R. Engels, et al., Measurement of the nuclear polarization of hydrogen and deuterium molecules using a lamb-shift polarimeter, Rev. Sci. Instrum. 85 (2014) 103505.
[34] R.J. Gould, E.E. Salpeter, The interstellar abundance of the hydrogen molecule, I. Basic Processes. Astrophys. J. 138 (1963) 393.
[35] G. Vidali, et al., Formation of molecular hydrogen on analogues of interstellar dust grains: experiments and modelling, in: Light, dust and chemical evolution, J. Phys.: Conf. Ser. 6 (2005) 36.
[36] H.C. van de Hulst, Recherches astronomiques de l'observatoire d'utrecht 11, 1946, parts I.
[37] M. Bonfanti, et al., Physisorption and diffusion of hydrogen atoms on graphite from correlated calculations on the H-coronene model system, J. Phys. Chem. C 111 (16) (2007) 5825–5829.
[38] L. Hornekær, et al., Metastable structures and recombination pathways for atomic hydrogen on the graphite (0001) surface, Phys. Rev. Lett. 96 (2006) 156104.
[39] S. Casolo, et al., Hydrogen recombination and dimer formation on graphite from ab inito molecular dynamics simulations, J. Phys. Chem. A 120 (27) (2016) 5032–5040.
[40] R. Frigge, Desorption of Molecular Hydrogen from HOPG (0001) Induced By Femtosecond Laser Pulses Dissertation, 2017, WWU Münster.
[41] I. Alata, et al., Vacuum ultraviolet photolysis of hydrogenated amorphous carbons, Astron. Astrophys. 569 (2014) A119.